Sensors & Diagnostics

PAPER

View Article Online
View Journal | View Issue

Cite this: *Sens. Diagn.*, 2022, **1**, 550

Nanostructured zirconia@reduced graphene oxide based ultraefficient nanobiosensing platform for food toxin detection†

Dipti Chauhan,‡[a] Yogesh Kumar,‡[a] Ramesh Chandra[ab] and Suveen Kumar *[a]

In this work, we report zirconia nanoparticle (~17 nm) decorated reduced graphene oxide nanocomposite ($nZrO_2$@RGO) based nanobiosensing platform for label-free and efficient detection of food toxin (aflatoxin B1, AFB1). A simple hydrothermal approach was followed for the synthesis of the $nZrO_2$@RGO nanocomposite, which was further functionalized with 3-aminopropyltriethoxy silane (APTES) and made to adhere electrophoretically onto an indium tin oxide (ITO) coated glass substrate (15 V, 180 s). The immobilization of monoclonal antibodies of aflatoxin B1 (anti-AFB1) and bovine serum albumin (BSA) was achieved through EDC–NHS chemistry and drop-casting method, respectively. The structural, morphological, and electrochemical attributes of $nZrO_2$@RGO and the fabricated bioelectrodes were characterized by spectroscopic, microscopic and electrochemical (cyclic voltammetry and differential pulse voltammetry) techniques. Here, the large surface area of RGO support helps in increasing the dispersibility of $nZrO_2$ which imparts synergistic effects to the $nZrO_2$@RGO nanocomposite and as result, accelerates the electron transfer process. Thus, the fabricated immunoelectrode (BSA/anti-AFB1/APTES/$nZrO_2$@RGO/ITO) efficiently detects AFB1 covering wider linear detection range between 1.5–18 ng mL^{-1} with lower limit of detection of 2.54 ng mL^{-1} and durability of 49 days.

Received 21st January 2022,
Accepted 26th March 2022

DOI: 10.1039/d2sd00012a

rsc.li/sensors

1. Introduction

Aflatoxins are toxic metabolites originating from the molds *Aspergillus flavus* and *Aspergillus parasiticus* that breed on food.[1] Worldwide, they have been associated with various diseases such as aflatoxicosis, chronic hepatitis, Reye's syndrome, cirrhosis, and carcinoma of liver in animals and humans. Aflatoxins have received more attention than other mycotoxins owing to their proven hazardous effects (carcinogenic and toxicological) in animals and humans. Among the 20 different varieties of aflatoxins, aflatoxin B1 (AFB1) is the most toxic natural hepatocarcinogen.[1] The acceptable concentration of AFB1 in food for human consumption is 2 μg kg^{-1}, beyond which it may lead to several chronic diseases including hepatocellular carcinoma.[1,2] The existing analytical techniques to detect AFB1 are thin-layer chromatography,[1,3] high performance liquid chromatography,[2,4] immunoaffinity column assay,[5,6] enzyme-linked immunosorbent assay,[1,7] *etc.* However, these methods are highly sophisticated, expensive, time-consuming and require large amount of samples.[2,8,9] To overcome these limitations, we require a more rapid, authentic, simple, and cost-effective technique for AFB1 detection. In this context, electrochemical nanobiosensors for food toxin detection have triggered high research interest owing to their excellent sensitivity, simplicity, high signal power to noise power ratio, and short output time.[2,10]

The role of the immobilization matrix in the development of a nanobiosensing platform is inevitable. Various metal oxides such as ZnO,[11] TiO_2,[12] Fe_3O_4,[13] MgO,[13] *etc.* have secured a profound position as an effective matrix support. Among these, nanostructured zirconia ($nZrO_2$) has recently sparked a lot of scientific interest among researchers, given its high surface area to volume ratio,[14] biocompatibility,[15] excellent electrochemical properties,[16] chemical inertness,[17] and high adsorption ability;[18] thus it can be effectively exploited for high loading of biomolecules with desired orientation. Furthermore, $nZrO_2$ also enables covalent attachment of silane groups and hydroxyl groups present on organosilanes (such as APTES) and ITO, respectively.[19,20] However, various studies have reported that $nZrO_2$ tends to congregate and form huge clusters.[20] Keeping this in view, a high surface area substrate could provide a suitable support for homogeneous dispersion of metal oxides.[20,21]

2D materials have risen as potential candidates that act as a high surface area substrate for dispersing metal oxides.

[a] *Department of Chemistry, University of Delhi, Delhi-110007, India. E-mail: suveendev@gmail.com*
[b] *Institute of Nano Medical Sciences, University of Delhi, Delhi-110007, India*

† Electronic supplementary information (ESI) available. See DOI: https://doi.org/10.1039/d2sd00012a

‡ These authors equally contributed to the work.

Studies have been directed in the past on graphene and its derivatives like graphene oxide, reduced graphene oxide (RGO), *etc.* as sensing materials.[22] Among these, RGO, which is appended through various oxygen containing functional groups, has shown immense potential in the development of nanobiosensing platforms due to its unique properties such as excellent heterogeneous electron transfer,[23] remarkable conductivity,[24] good mechanical flexibility,[25] high catalytic activity, and capability to facilitate direct electron transfer across the electrode surface.[26,27] The high surface area of RGO may assist in dispersing metal oxides, thus preventing the agglomeration of nanoparticles. The dispersed metal oxide on the RGO sheet will be helpful in reducing steric hindrance produced between the biomolecules.[28–30] Also, the electrochemical performance is known to be enhanced when using a conductive and large surface area support for metal oxides.[20,21,30] A RGO supported $nZrO_2$ nanoparticle based biosensing platform has been successfully employed for enzyme immobilization and utilized for chlorpyrifos pesticide detection.[21] Gupta *et al.* showed an improvement in electrochemical characteristics and low aggregation of ZrO_2 nanoparticles by employing a ZrO_2-RGO nanocomposite for the detection of ochratoxin A.[31] In another work, a well-dispersed zirconia decorated RGO has been utilized as an efficient immobilization matrix for the detection of oral cancer.[20] Along with this, these 2D materials have been significantly used for the development of point-of-care devices, attributed to their tailor-made physical and chemical properties, remarkable mechanical strength, favorable flexibility, and so on. In several studies, 2D material-based biosensors have been utilized to detect different metabolic imperfections and environmental risk factors, including pathogens and toxins.[22,32] With these considerations in mind, $nZrO_2$–RGO nanocomposite seems to be a highly efficient immobilization matrix for the development of a nanobiosensing platform in which both components synergistically compensate for each other's shortcomings.

In the present work, we report a label free immunosensor based on APTES functionalized $nZrO_2$@RGO nanocomposite for AFB1 detection. The demonstrated method is economical and simple that involves direct immobilization of antibodies onto the $nZrO_2$@RGO nanocomposite. This fabricated $nZrO_2$@RGO immunosensor exhibits wider linear detection range (1.5–18 ng mL^{-1}) which covers the permitted as well as lethal levels of AFB1 concentration. Along with this, high durability of up to 49 days was achieved. To the best of our knowledge, this is the first report on food toxin (AFB1) detection based on a $nZrO_2$@RGO based nanocomposite.

2. Experimental details

2.1. Synthesis of graphene oxide (GO)

Natural graphite flakes were used for the synthesis of GO using a method proposed by Kumar *et al.*[20] Briefly, 0.5 g of natural graphite flakes were placed in a round-bottom flask and mixed with 12 mL of H_2SO_4 followed by continuous vigorous stirring at 0 °C for 2 h. Next, 1.5 g of $KMnO_4$ was added to the solution, maintaining it at ice cold temperature. Further, the temperature was raised to 35 °C for the next 4 h followed by addition of 30 mL of deionised water for another 2 h. Then, H_2O_2 (30%) was added dropwise until the reaction solution turned yellow with subsequent addition of HCl (5% by volume), till the solution turned brown due to removal of excess manganese salt. The final obtained product was washed with deionised water until pH reached neutral, then dried at 60 °C and stored in a dry place.

2.2. Synthesis and functionalization of the $nZrO_2$@RGO nanocomposite

A low temperature hydrothermal method was used for the *in situ* synthesis of $nZrO_2$@RGO nanocomposite. Initially, 100 mg of GO was thoroughly dispersed in 40 mL Milli-Q water for 1 h and this was added into a 10 mL aqueous solution of $Zr(OC_2H_5)_4$ (0.01 M) with vigorous stirring. After 2 h of stirring, 10 mL of 0.08 M NaOH solution was added for the conversion of GO to RGO and zirconium ethoxide to zirconium hydroxide. Thereafter, CTAB (0.01 M, 10 mL) solution was added and stirred for 2 h to avoid coagulation of nanostructured molecules. Lastly, the solution was kept in a hydrothermal pressure tank at 165 °C for 17 h. The obtained grey precipitate was washed using deionized water till the solution became neutral, dried at 60 °C overnight, and kept in a dry place for storage.

For functionalization of the synthesized $nZrO_2$@RGO nanocomposite, 50 mg of $nZrO_2$@RGO was dispersed in isopropanol (1 mg mL^{-1}) at 60 °C with continuous stirring (300 rpm). Thereafter, APTES (98%, 200 μL) was added dropwise with subsequent addition of Milli-Q water (5 mL), and the solution was allowed to stir for the next 48 h. The obtained product (APTES/$nZrO_2$@RGO) was filtered out through Whatman filter paper, dried at 70 °C for 4 h, and then stored in a dry place.

2.3. Fabrication of the nanobiosensing platform

Firstly, hydrolysis of ITO coated glass substrates was executed using a $H_2O_2 : NH_4OH : H_2O$ solution (1 : 1 : 5) at 80 °C for 30 min. For electrophoretic deposition (EPD), the APTES/$nZrO_2$@RGO functionalized nanocomposite was dispersed in acetonitrile (0.4 mg mL^{-1}) through ultrasonication. Further $Mg(NO_3)_2{\cdot}6H_2O$ was used to enhance the surface charge. A conventional two electrode system comprising ITO and Pt as the cathode and anode, respectively, having separation distance of 1 cm was employed, and thin film of APTES/$nZrO_2$@RGO was obtained onto prehydrolyzed ITO substrate at DC potential of 15 V for 180 s. For anti-AFB1 antibody immobilization, solution (30 μL) of 0.2 M EDC (coupling agent), 0.05 M NHS (activator), and 50 μg mL^{-1} anti-AFB1 was prepared in 1 : 1 : 2 ratio and kept for 30 min; this was subsequently spread onto the APTES/$nZrO_2$@RGO/ITO electrode. Finally, after washing with phosphate buffer saline (PBS), 20 μL of BSA was employed

to reduce non-specific attachment of AFB1. The fabricated BSA/anti-AFB1/APTES/$nZrO_2$@RGO/ITO immunoelectrode was then stored at 4 °C till further use after washing with PBS. A schematic representation of the fabrication steps of the BSA/anti-AFB1/APTES/$nZrO_2$@RGO/ITO immunoelectrode is shown in Scheme 1.

3. Results and discussion

3.1. Structural and morphological studies

The skeletal structure of the $nZrO_2$@RGO nanocomposite was investigated by X-ray diffraction (XRD) studies. Fig. 1(a) shows the XRD pattern of the hydrothermally synthesized $nZrO_2$@RGO nanocomposite obtained at 2θ angles between 20–70°. The intense peak seen at 24.10° is due to the merging of $nZrO_2$ (011, monoclinic phase) and RGO (002) planes. Peaks observed at 28.30°, 34.43°, 41.08°, 45.29°, and 55.37° correspond to the ($\bar{1}11$), (020), (102), ($\bar{2}02$), and (013) planes of the monoclinic phase [JCPDS: 89-9066] whereas peaks at 30.29°, 50.26°, and 60.05° correspond to the (101), (112) and (211) planes of the tetragonal phase [JCPDS: 80-2155] of $nZrO_2$, respectively. The low intensity peak seen at 43.00° indexed as the (001) plane is due to RGO. The XRD results indicate the synthesis of mixed-phase zirconia nanoparticles with RGO. The mean grain size (D) of zirconia in the prepared nanocomposite ($nZrO_2$@RGO) was computed to be ~5 nm by using Scherer's formula ($D = 0.94\lambda/\beta \cos\theta$),[33] where λ represents the X-ray wavelength which is 1.54 Å, β denotes the full width at half maximum, and θ signifies Bragg's angle. The calculated crystallite size indicates successful formation of nanostructured zirconia.

To study the morphological properties of $nZrO_2$@RGO nanocomposite, SEM and TEM results were recorded. For this, the $nZrO_2$@RGO nanocomposite was dispersed in Milli-Q water and drop-cast onto an ITO substrate for SEM viewing. The obtained results are shown in Fig. 1(b). It clearly appears that the nanostructured $nZrO_2$ is grafted onto the RGO sheet. For TEM imaging, the $nZrO_2$@RGO nanocomposite was dispersed in ethanol and drop-cast onto a carbon coated gold grid. Fig. 1(c and d) show the TEM images, indicating the uniform decoration of nanostructured $nZrO_2$ onto the RGO sheet as compared to $nZrO_2$ without RGO,[19,34,35] thus indicating formation of highly dispersed $nZrO_2$. The average particle size of $nZrO_2$ was calculated to be ~17 nm, which clearly indicates the formation of nanostructured zirconia onto the RGO surface.

3.2. Fourier transform infrared spectroscopy (FT-IR) studies

To investigate the functional group modifications in GO, the FT-IR spectra of GO and $nZrO_2$@RGO were analyzed, and obtained results are shown in Fig. S1(a and b).† The characteristic peaks of various oxygen functionalities are

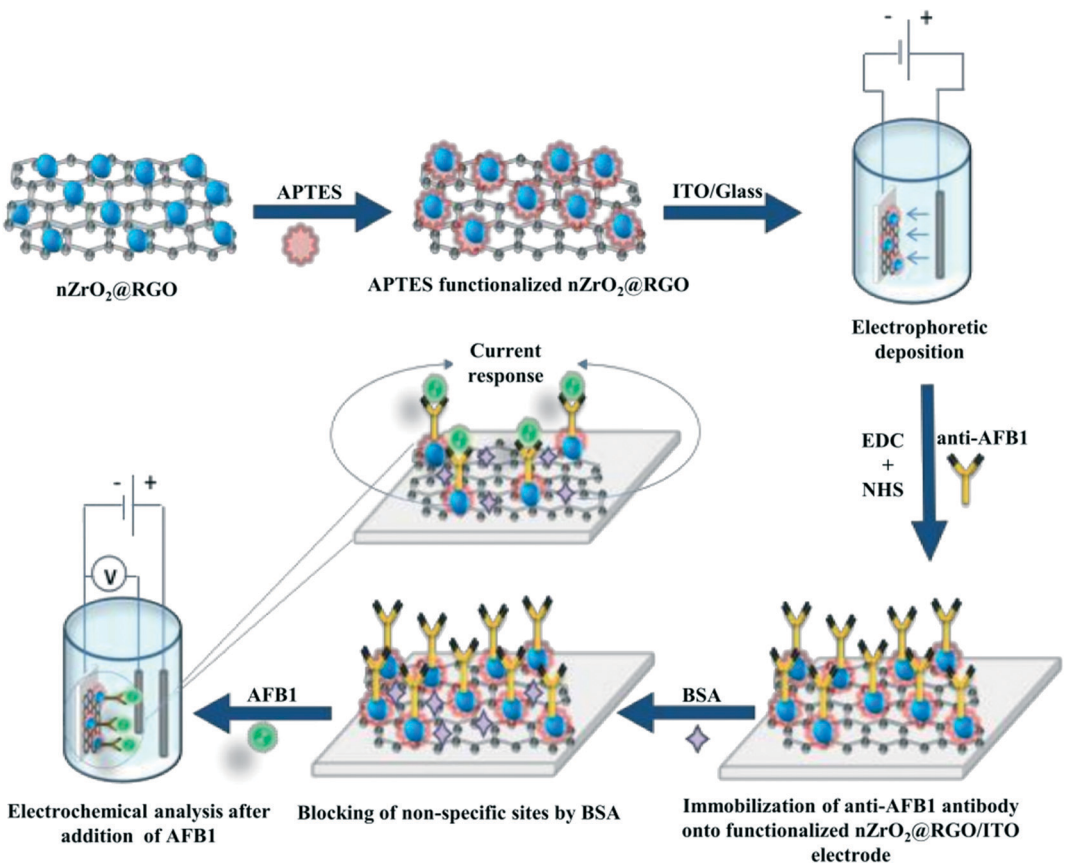

Scheme 1 Schematic representation of the fabrication steps of the BSA/anti-AFB1/APTES/$nZrO_2$@RGO/ITO immunoelectrode.

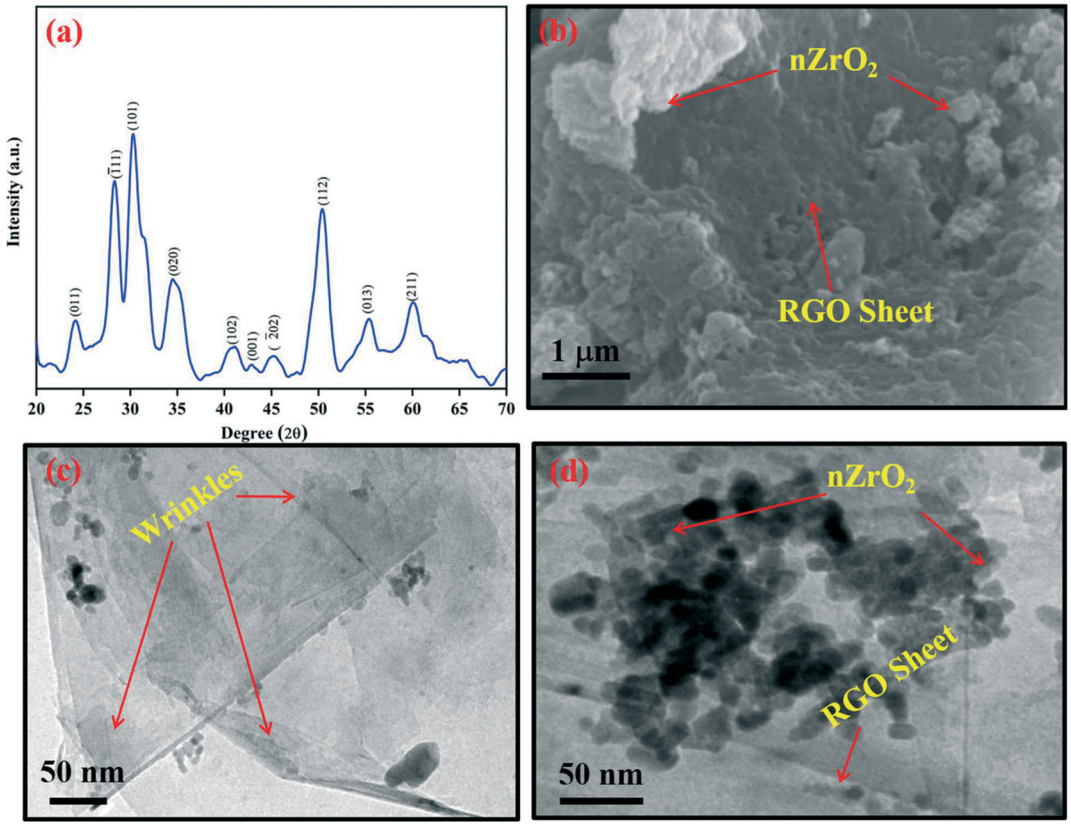

Fig. 1 (a) XRD spectrum of the synthesized $nZrO_2$@RGO nanocomposite; (b) SEM and (c and d) TEM images of the $nZrO_2$@RGO nanocomposite.

observed in the 1793–1752 cm^{-1} region, corresponding to carboxyl species having C=O stretching. However, the peaks observed between 2447–2412 cm^{-1} corresponding to CO_2 stretching are absent in the second curve. Along with this, the peaks at 1604 cm^{-1}, 1278 cm^{-1} and 1072 cm^{-1} are prominent in GO due to the presence of O–H bending, epoxy C–O stretching, and alkoxy C–O stretching, respectively, which gets diminished in RGO.[36,37] This confirms the successful reduction of GO to RGO. Further, to examine the presence of functionalities in APTES/$nZrO_2$@RGO/ITO and anti-AFB1/APTES/$nZrO_2$@RGO/ITO electrodes, their FT-IR spectra were recorded and the obtained results are shown in Fig. S2(a and b).† In (a) APTES/$nZrO_2$@RGO/ITO, the bands present at 3300 cm^{-1} and 1540 cm^{-1} are ascribed to the free amine groups on the exterior of the APTES/$nZrO_2$@RGO/ITO electrode. The peak positioned at 1106 cm^{-1} corresponds to the stretching vibration of C–OH onto the RGO sheet. In (b) anti-AFB1/APTES/$nZrO_2$@RGO/ITO, the broad peak found at 1029 cm^{-1} indicates the amide bond [C(O)–NH] formation between the amine and carboxyl groups present on the APTES/$nZrO_2$@RGO/ITO electrode and anti-AFB1 antibodies, respectively, thus confirming the successful covalent immobilization of biomolecules.[38]

3.3. Electrochemical studies

The electrochemical attributes of the fabricated electrodes were studied through cyclic voltammetry (CV) and differential pulse voltammetry (DPV) in PBS solution (5 mM, 0.9% NaCl, pH 7.0) comprising $[Fe(CN)_6]^{3-/4-}$ as redox species. To study the effect of pH (6.0–8.0) on the electrochemical properties of the developed nanobiosensing platform (BSA/anti-AFB1/APTES/$nZrO_2$@RGO/ITO), the DPV response was recorded at varying potential from −0.2 V to +0.6 V. As is evident from Fig. 2(a), the maximum peak current is observed at pH 7.0, which may be due to the fact that at neutral pH the antibodies are present in natural form with the highest activity, tending to get denatured in acidic or basic medium.[27] Thus, for further electrochemical studies, PBS buffer with pH 7.0 was used.

Further, to investigate the changes in the peak current at different steps of the electrode modification, the electrochemical response of APTES/$nZrO_2$@RGO/ITO, anti-AFB1/APTES/$nZrO_2$@RGO/ITO and BSA/anti-AFB1/APTES/$nZrO_2$@RGO/ITO electrodes were recorded through DPV (potential range: −0.2 V to +0.6 V) and the obtained results are shown in Fig. 2(b). It is observed that the anodic peak current of the APTES/$nZrO_2$@RGO/ITO electrode (0.102 mA) lowers to 0.099 mA after anti-AFB1 immobilization. This may be credited to the obstruction in the electron transfer as the redox active sites are being deeply entrapped into the macromolecular structure of antibodies.[28] The peak current further decreases to a value of 0.090 mA after the non-specific sites on the anti-AFB1/APTES/$nZrO_2$@RGO/ITO electrode are blocked using BSA due to its insulating nature.[19]

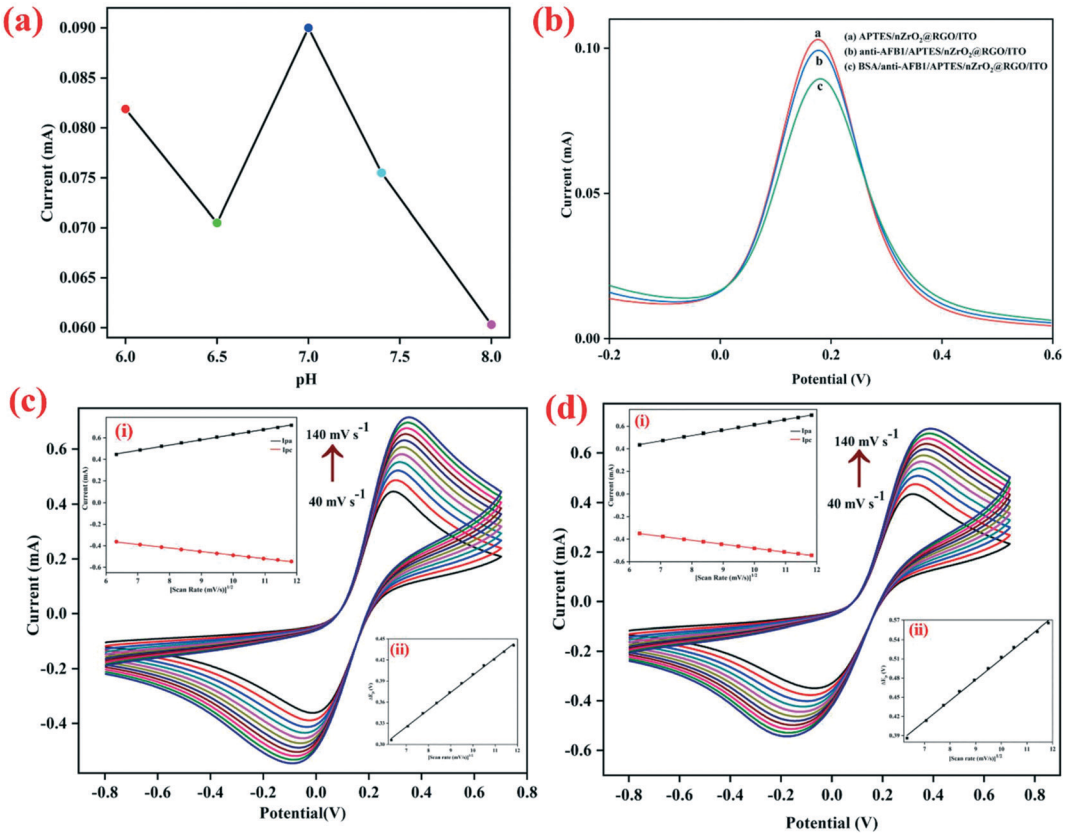

Fig. 2 (a) Electrochemical response of the BSA/anti-AFB1/APTES/$nZrO_2$@RGO/ITO immunoelectrode with respect to pH (ranging from 6.0–8.0). (b) Differential pulse voltammetry (DPV) studies of APTES/$nZrO_2$@RGO/ITO, anti-AFB1/APTES/$nZrO_2$@RGO/ITO, and BSA/anti-AFB1/APTES/$nZrO_2$@RGO/ITO electrodes. Cyclic voltammetry (CV) curves of (c) APTES/$nZrO_2$@RGO/ITO and (d) BSA/anti-AFB1/APTES/$nZrO_2$@RGO/ITO electrodes as a function of the scan rate (40–140 mV s^{-1}); insets (i): magnitude of oxidation and reduction peak currents as a function of the square root of the scan rate and insets (ii): difference between the cathodic and anodic peak potential (ΔE_p) as a function of the square root of the scan rate.

Furthermore, the interfacial kinetics of the BSA/anti-AFB1/APTES/$nZrO_2$@RGO/ITO and APTES/$nZrO_2$@RGO/ITO electrodes was examined through CV (potential range: −0.8 V to +0.8 V) by studying the variation in peak current values as a function of varying scan rates (40–140 mV s^{-1}), as shown in Fig. 2(c and d). As seen in the figures, the magnitude of the peak currents (both anodic, I_{pa}, and cathodic, I_{pc}) follows a linear increasing trend against the square root of the scan rate ($\upsilon^{1/2}$) (inset (i), Fig. 2(c and d)) which signifies that the electrochemical process is diffusion controlled[26,39] and follows eqn (S1) to (S4).† Further, the I_{pa} and I_{pc} values also shift to more positive and negative potentials, respectively, on stepping up the sweep rate. The difference in magnitude of the redox peak potentials ($\Delta E_p = E_{pa} - E_{pc}$) shows linear variation with $\upsilon^{1/2}$, where E_{pc} and E_{pa} represent the cathodic and anodic peak potentials, respectively. The obtained results are shown in inset (ii), Fig. 2(c and d), indicating the facile charge transfer kinetics between the medium and the electrode interface[27] which follows eqn (S5) and (S6).† Furthermore, the surface concentration (γ) of the BSA/anti-AFB1/APTES/$nZrO_2$@RGO/ITO electrode was computed to be 7.6×10^{-9} mol cm^{-2} by applying the Brown–Anson equation, eqn (i):[40]

$$I_p = n^2F^2\gamma A\upsilon(4RT)^{-1} \quad \text{(i)}$$

where I_p shows the peak current of the immunoelectrode, n denotes the number of electrons transferred for $[Fe(CN)_6]^{3-/4-}$ (n = 1), F represents the Faraday constant (96 485 C mol^{-1}), A signifies the electrode surface area (0.25 cm^2), R represents the gas constant (8.314 J mol^{-1} K^{-1}), υ denotes the sweep/scan rate (V s^{-1}), and T is the room temperature (298 K or 25 °C).

The diffusion coefficient (D) of the BSA/anti-AFB1/APTES/$nZrO_2$@RGO/ITO electrode was evaluated to be 1.13×10^{-3} cm^2 s^{-1} by applying the Randles–Ševčík equation, eqn (ii):[29]

$$I_p = (2.69 \times 10^5)n^{3/2}AD^{1/2}C\upsilon^{1/2} \quad \text{(ii)}$$

where C signifies the concentration of redox species (5×10^{-3} mol cm^{-2}) and the other terms are as described above.

3.4. Electrochemical response studies

The electrochemical response signal of the BSA/anti-AFB1/APTES/$nZrO_2$@RGO/ITO bioelectrode was recorded by increasing the concentration of the AFB1 antigen (1.5–18 ng mL^{-1}) using DPV (potential range: −0.2 V to +0.6 V) and the results are shown in

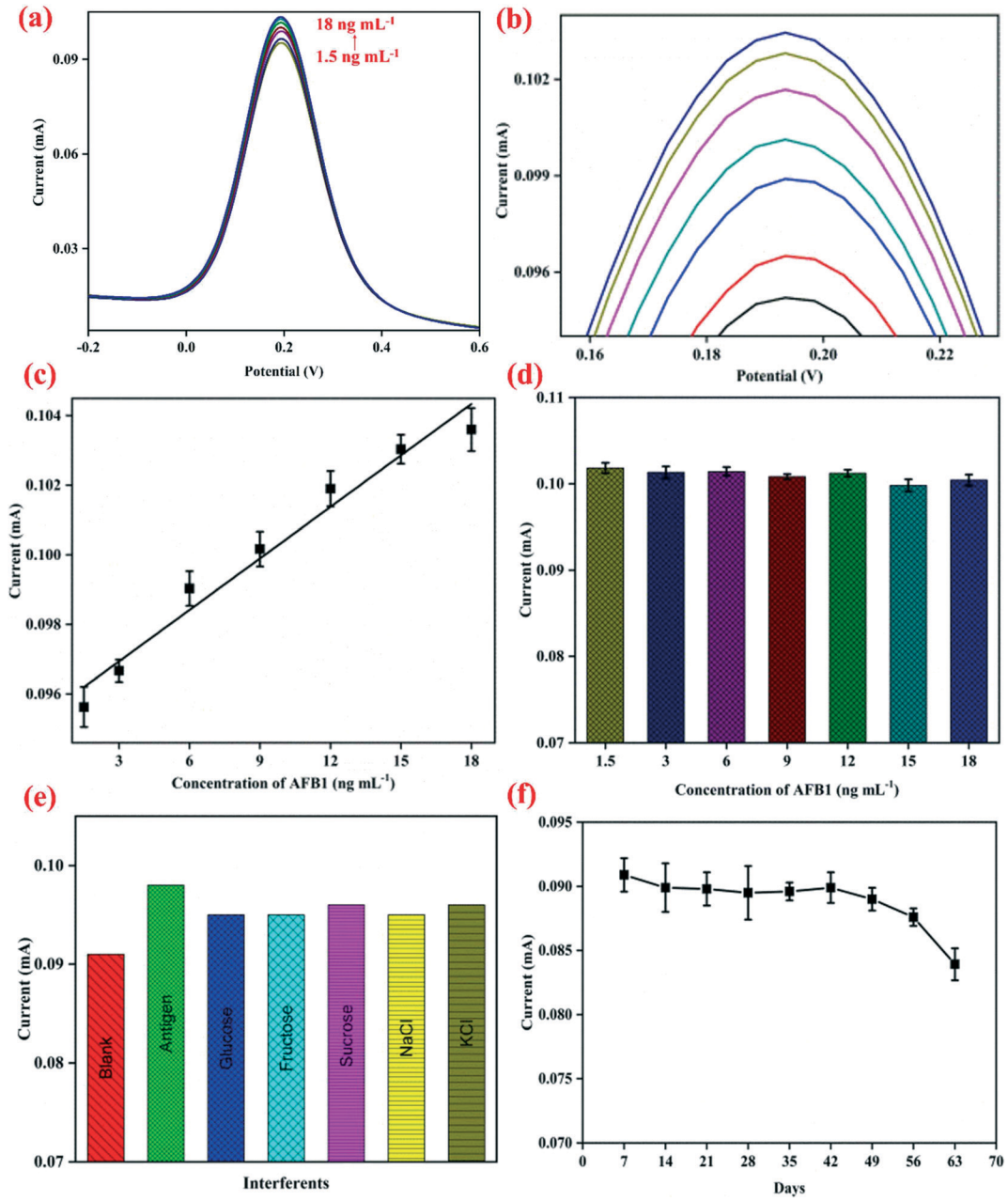

Fig. 3 (a) Electrochemical response signal of the BSA/anti-AFB1/APTES/$nZrO_2$@RGO/ITO electrode against AFB1 concentration (1.5–18 ng mL^{-1}) using DPV; (b) enlarged view of the anodic peak current, (c) calibration plot of the anodic peak current *vs.* the concentration of AFB1 (1.5–18 ng mL^{-1}), (d) control experiment of the APTES/ZrO_2@RGO/ITO electrode against AFB1 concentration (1.5–18 ng mL^{-1}), (e) interferent studies of the BSA/anti-AFB1/APTES/$nZrO_2$@RGO/ITO electrode against AFB1 in the presence of various analytes present in food samples, and (f) durability studies of the BSA/anti-AFB1/APTES/$nZrO_2$@RGO/ITO electrode.

Fig. 3(a) with enlarged view in Fig. 3(b). After addition of each concentration of AFB1, an incubation time of 20 min was given for proper binding of the antigen with the immunoelectrode. It is inferred that the value of the peak current increases proportionally in a linear fashion with increasing AFB1 concentration, as shown in Fig. 3(c), and follows eqn (iii):

$$I_p\ (\text{mA}) = [0.0005 \pm (3.86 \times 10^{-5})\ \text{mA ng}^{-1}\ \text{mL}] \times \text{conc. of AFB1 (ng mL}^{-1}) + (0.095 \pm 0.0004)$$
$$R^2 = 0.97 \quad \text{(iii)}$$

This increment in the value of the peak current can be ascribed to the immunocomplex formed on the surface of electrode which promotes facile electron transfer process.[19] The fabricated nanobiosensor covers linear range starting from 1.5 ng mL^{-1} to 18 ng mL^{-1} which covers the permitted as well as lethal levels of AFB1, which is much wider than that of the graphene quantum dots–gold nanoparticles composite,[41] carboxylated MWCNTs,[2] graphitic carbon nitride[10] based, and other nanobiosensors reported so far.[42–44] This wide detection range may be due to the defects

Table 1 A comparative investigation of the biosensing parameters of existing nanobiosensors for AFB1 detection with the current work

S. No.	Detection technique	Materials used	LDR (ng mL^{-1})	LOD (ng mL^{-1})	Durability (days)	Ref.
1.	CV, EIS	SPEs	50×10^{-6} to 5	50×10^{-6}	—	44
2.	DPV	PTH/AuNP/GCE	0.6 to 2.4	0.07	—	43
3.	CV, DPV	C-AuNP/MBA/Au	0.1 to 1	0.1790	—	42
4.	CV	c-MWCNTs/ITO	0.25 to 1.375	0.08	45	2
5.	CV	GQDs-AuNPs/ITO	0.1 to 3.0	0.008	56	41
6.	CV	Thn/g-C_3N_4/ITO	1×10^{-6} to 1	0.328	49	10
7.	**DPV**	**APTES/nZrO_2@RGO/ITO**	**1.5 to 18**	**2.54**	**49**	**Current work**

Abbreviations used – CV: cyclic voltammetry, DPV: differential pulse voltammetry, EIS: electrochemical impedance spectroscopy, SPE: screen printed electrode, PTH: polythionine, AuNP: gold nanoparticle, GCE: glassy carbon electrode, MBA: mercaptobenzoic acid, MWCNTs: multi-walled carbon nanotubes, GQDs: graphene quantum dots, Thn: thionine, g-C_3N_4: graphitic carbon nitride, APTES: 3-aminopropyltriethoxysilane, nZrO_2@RGO: zirconia@reduced graphene oxide nanocomposite, ITO: indium tin oxide.

and oxygenated groups present on the nZrO_2 surface uniformly dispersed over RGO that leads to a larger electrochemically active surface area for the adsorption of biomolecules. Moreover, the synergistic properties of nZrO_2 and RGO accelerate the electron transfer process, providing good electrocatalytic effect of oxidation/reduction of protein.[19,20] The positive slope of the calibration plot was used to calculate the sensitivity of the immunoelectrode to be 1.97 μA ng^{-1} mL cm^{-2}. The limit of detection (LOD)[45] was determined to be 2.54 ng mL^{-1} by applying eqn (iv):

$$\mathrm{LOD} = 3\sigma_b/m \quad \text{(iv)}$$

where σ_b and m represent the standard deviation of the intercept and the slope of curve, respectively. The obtained LOD is much lower than that of Fe_3O_4/GO[46] and MnO_2[47] based biosensors reported so far. A comparative investigation of the biosensing parameters of existing nanobiosensors for AFB1 detection and the current work is displayed in Table 1.

To investigate the cross-reactivity of the APTES/nZrO_2@RGO/ITO electrode with AFB1, a control experiment was performed by studying the electrochemical signals of the APTES/nZrO_2@RGO/ITO electrode at increasing concentrations (1.5–18 ng mL^{-1}) of AFB1. It is clear from Fig. 3(d) that no significant change in anodic peak current values was observed on increasing the concentration of AFB1, indicating that the APTES/nZrO_2@RGO/ITO electrode surface doesn't interact with antigen molecules. Therefore, the root cause of increasing current in response studies was the immunoreaction between the BSA/anti-AFB1/APTES/nZrO_2@RGO/ITO electrode and the AFB1 antigen. To evaluate the selectivity of the immunoelectrode, interferent studies were conducted with several analytes such as glucose, fructose, sucrose, NaCl, $MgCl_2$, *etc.* present in food, and the obtained results are shown in Fig. 3(e). The immunosensor was incubated with a solution of 5 ng mL^{-1} AFB1 containing one of the above analytes, and it was found that no substantial change occurred in the anodic peak current in the presence of various analytes, indicating the fabricated immunoelectrodes exhibit good selectivity. The durability of the fabricated nanobiosensor (BSA/anti-AFB1/APTES/nZrO_2@RGO/ITO) was investigated through CV at a regular interval of 7 days and the obtained results are shown in Fig. 3(f). It is observed that it sustains 95% of the current value till 49 days; thereafter, it decreases marginally to 80% at the end of 56 days. Thus, the fabricated nanobiosensor exhibits a durability of 49 days.

4. Conclusions

We demonstrate a label free immunosensor based on a nZrO_2@RGO nanocomposite for AFB1 detection. The synergistic effect of the intriguing properties of nZrO_2 and RGO helps to enhance the electrochemical parameters. Moreover, the presence of RGO reduces the agglomeration of zirconia nanoparticles by providing high surface area support. The use of this nanocomposite helps in achieving wider linear detection range (1.5–18 ng mL^{-1}) which covers the permitted as well as lethal levels of AFB1 and low limit of detection (2.54 ng mL^{-1}). Along with this, the fabricated nanobiosensor exhibits a high durability of 49 days. The synthesized nanocomposite holds enormous potential for the fabrication of nanobiosensors for the detection of other food toxins as well as for biomedical applications. More attempts ought to be made to investigate the performance of the fabricated nanobiosensor with real food samples.

Author contributions

Dipti Chauhan: formal analysis, investigation, writing – original draft. Yogesh Kumar: formal analysis, investigation, writing – original draft. Ramesh Chandra: writing – review & editing. Suveen Kumar: conceptualization, methodology, supervision, validation, writing – review & editing.

Conflicts of interest

There are no conflicts of interest to declare.

Acknowledgements

The authors thank the Vice Chancellor, University of Delhi, Delhi (India) for providing the research facilities. DC and YK thank the UGC fellowship (191620082661 and 99/

CSIRNETJUNE2019, respectively) for financial support. SK acknowledges the DST-INSPIRE Faculty scheme (DST/INSPIRE/04/2017/001336) and the Institution of Eminence, University of Delhi (IoE/2021/12/FRP) for financial support. The authors also thank the University Science Instrumentation Centre (USIC) for providing the necessary instrumental facilities.

References

1 S. J. Daly, G. J. Keating, P. P. Dillon, B. M. Manning, R. O'Kennedy, H. A. Lee and M. R. Morgan, *J. Agric. Food Chem.*, 2000, **48**, 5097–5104.
2 C. Singh, S. Srivastava, M. A. Ali, T. K. Gupta, G. Sumana, A. Srivastava, R. B. Mathur and B. D. Malhotra, *Sens. Actuators, B*, 2013, **185**, 258–264.
3 I. Var, B. Kabak and F. Gök, *Food Control*, 2007, **18**, 59–62.
4 Y. Rodríguez-Carrasco, L. Izzo, A. Gaspari, G. Graziani, J. Mañes and A. Ritieni, *Beverages*, 2018, **4**, 43.
5 E. Dinckaya, O. Kinik, M. K. Sezginturk, C. Altug and A. Akkoca, *Biosens. Bioelectron.*, 2011, **26**, 3806–3811.
6 M. Ardic, Y. Karakaya, M. Atasever and H. Durmaz, *Food Chem. Toxicol.*, 2008, **46**, 1596–1599.
7 B. H. Liu, Y. T. Hsu, C. C. Lu and F. Y. Yu, *Food Control*, 2013, **30**, 184–189.
8 A. K. Singh, T. K. Dhiman, G. Lakshmi and P. R. Solanki, *Bioelectrochemistry*, 2021, **137**, 107684.
9 M. Kundu, H. Bhardwaj, M. K. Pandey, P. Krishnan, R. Kotnala and G. Sumana, *J. Food Sci. Technol.*, 2019, **56**, 1829–1840.
10 V. Nirbhaya, D. Chauhan, R. Jain, R. Chandra and S. Kumar, *Bioelectrochemistry*, 2021, **139**, 107738.
11 A. Tamashevski, Y. Harmaza, R. Viter, D. Jevdokimovs, R. Poplausks, E. Slobozhanina, L. Mikoliunaite, D. Erts, A. Ramanaviciene and A. Ramanavicius, *Talanta*, 2019, **200**, 378–386.
12 Z. D. Gao, F. F. Guan, C. Y. Li, H. F. Liu and Y. Y. Song, *Biosens. Bioelectron.*, 2013, **41**, 771–775.
13 P. R. Solanki, A. Kaushik, V. V. Agrawal and B. D. Malhotra, *NPG Asia Mater.*, 2011, **3**, 17–24.
14 V. G. Deshmane and Y. G. Adewuyi, *Microporous Mesoporous Mater.*, 2012, **148**, 88–100.
15 P. K. Gupta, N. Pachauri, Z. H. Khan and P. R. Solanki, *J. Electroanal. Chem.*, 2017, **807**, 59–69.
16 H.-L. Chu, W.-S. Hwang, J.-K. Du, K.-K. Chen and M.-C. Wang, *J. Alloys Compd.*, 2016, **678**, 518–526.
17 R. Hannink, M. Murray and H. Scott, *Wear*, 1984, **100**, 355–366.
18 C. Piconi and G. Maccauro, *Biomaterials*, 1999, **20**, 1–25.
19 S. Kumar, S. Kumar, S. Tiwari, S. Srivastava, M. Srivastava, B. K. Yadav, S. Kumar, T. T. Tran, A. K. Dewan, A. Mulchandani, J. G. Sharma, S. Maji and B. D. Malhotra, *Adv. Sci.*, 2015, **2**, 1500048.
20 S. Kumar, J. G. Sharma, S. Maji and B. D. Malhotra, *Biosens. Bioelectron.*, 2016, **78**, 497–504.
21 N. K. Mogha, V. Sahu, M. Sharma, R. K. Sharma and D. T. Masram, *Mater. Des.*, 2016, **111**, 312–320.
22 V. Chaudhary, A. K. Kaushik, H. Furukawa and A. Khosla, *ECS Sensors Plus*, 2022, DOI: **10.1149/2754-2726/ac5ac6**.
23 S. Palanisamy, C. Karuppiah and S. M. Chen, *Colloids Surf., B*, 2014, **114**, 164–169.
24 C. Xu, X. Shi, A. Ji, L. Shi, C. Zhou and Y. Cui, *PLoS One*, 2015, **10**, e0144842.
25 A. Sumboja, C. Y. Foo, X. Wang and P. S. Lee, *Adv. Mater.*, 2013, **25**, 2809–2815.
26 C. Chaudhary, S. Kumar and R. Chandra, *Microchem. J.*, 2020, **159**, 105344.
27 D. Chauhan, Pooja, V. Nirbhaya, C. M. Srivastava, R. Chandra and S. Kumar, *Microchem. J.*, 2020, **155**, 104697.
28 S. Kumar, Ashish, S. Kumar, S. Augustine, S. Yadav, B. K. Yadav, R. P. Chauhan, A. K. Dewan and B. D. Malhotra, *Biosens. Bioelectron.*, 2018, **102**, 247–255.
29 S. Kumar, N. Gupta and B. D. Malhotra, *Bioelectrochemistry*, 2021, **140**, 107799.
30 G. Rathee, G. Bartwal, J. Rathee, Y. K. Mishra, A. Kaushik and P. R. Solanki, *Adv. NanoBiomed Res.*, 2021, **1**, 2100039.
31 P. K. Gupta, S. Tiwari, Z. H. Khan and P. R. Solanki, *J. Mater. Chem. B*, 2017, **5**, 2019–2033.
32 S. Roy, F. Arshad, S. Eissa, M. Safavieh, S. G. Alattas, M. U. Ahmed and M. Zourob, *Sens. Diagn.*, 2022, **1**, 87–105.
33 N. Rani, S. Chahal, A. S. Chauhan, P. Kumar, R. Shukla and S. Singh, *Mater. Today: Proc.*, 2019, **12**, 543–548.
34 M. R. H. Siddiqui, A. I. Al-Wassil, A. M. Al-Otaibi and R. M. Mahfouz, *Mater. Res.*, 2012, **15**, 986–989.
35 N. Pinna, *SPIE Newsroom*, 2009.
36 V. H. Pham, T. V. Cuong, S. H. Hur, E. Oh, E. J. Kim, E. W. Shin and J. S. Chung, *J. Mater. Chem.*, 2011, **21**, 3371–3377.
37 N. Sudesh, S. Kumar, C. Bernhard Das and G. Varma, *Supercond. Sci. Technol.*, 2013, **26**, 095008.
38 D. L. Pavia, G. M. Lampman, G. S. Kriz and J. Vyvyan, *Introduction to Spectroscopy*, Cengage learning, 2014.
39 V. Nirbhaya, C. Chaudhary, D. Chauhan, R. Chandra and S. Kumar, *New J. Chem.*, 2022, **46**, 6201–6211.
40 R. Nenkova, J. Wu, Y. Zhang and T. Godjevargova, *Anal. Biochem.*, 2013, **439**, 65–72.
41 H. Bhardwaj, M. K. Pandey, Rajesh and G. Sumana, *Microchim. Acta*, 2019, **186**, 592.
42 A. Sharma, Z. Matharu, G. Sumana, P. R. Solanki, C. G. Kim and B. D. Malhotra, *Thin Solid Films*, 2010, **519**, 1213–1218.
43 J. H. Owino, O. A. Arotiba, N. Hendricks, E. A. Songa, N. Jahed, T. T. Waryo, R. F. Ngece, P. G. Baker and E. Iwuoha, *Sensors*, 2008, **8**, 8262–8274.
44 Z. B. Abdallah, C. Grauby-Heywang, L. Beven, S. Cassagnere, F. Moroté, E. Maillard, H. Sghaier and T. C. Bouhacina, *Biochem. Eng. J.*, 2019, **150**, 107262.
45 R. Jain, V. Nirbhaya, R. Chandra and S. Kumar, *Electroanalysis*, 2021, **33**, 1–14.
46 W. Zhu, L. Li, Z. Zhou, X. Yang, N. Hao, Y. Guo and K. Wang, *Food Chem.*, 2020, **319**, 126544.
47 A. K. Singh, G. Lakshmi, T. K. Dhiman, A. Kaushik and P. R. Solanki, *Front. Nanotechnol.*, 2021, **2**, 23.